



## Satellite-derived SO<sub>2</sub> flux time-series and magmatic processes during the 2015 Calbuco eruptions

Federica Pardini<sup>1</sup>, Mike Burton<sup>1</sup>, Fabio Arzilli<sup>1</sup>, Giuseppe La Spina<sup>1</sup>, Margherita Polacci<sup>1</sup>

<sup>1</sup>School of Earth and Environmental Science, University of Manchester, Manchester, M13 9PL, UK

5 *Correspondence to:* Federica Pardini ([federica.pardini@manchester.ac.uk](mailto:federica.pardini@manchester.ac.uk))

**Abstract.** Quantifying time-series of sulphur dioxide (SO<sub>2</sub>) emissions during explosive eruptions provides insight into volcanic processes, assists in volcanic hazard mitigation, and permits quantification of the climatic impact of major eruptions. While volcanic SO<sub>2</sub> is routinely detected from space during eruptions, the retrieval of plume injection height and SO<sub>2</sub> flux time-series remains challenging. Here we present a new numerical method based on forward- and backward-  
10 trajectory analyses which enable such time-series to be robustly determined. The method is applied to satellite images of volcanic eruption clouds through the integration of the HYSPLIT software with custom-designed Python routines in a fully automated manner. Plume injection height and SO<sub>2</sub> flux time-series are computed with a period of ~10 minutes with low computational cost.

Using this technique, we investigated the SO<sub>2</sub> emissions from two sub-Plinian eruptions of Calbuco, Chile,  
15 produced in April 2015. We found a mean injection height above the vent of ~15 km for the two eruptions, with overshooting tops reaching ~20 km. We calculated a total of 300±46 kt of SO<sub>2</sub> released almost equally during both events, with 160±30 kt produced by the first event and 140±35 kt by the second. The retrieved SO<sub>2</sub> flux time-series show an intense gas release during the first eruption (average flux of 2560 kt day<sup>-1</sup>), while a lower SO<sub>2</sub> flux profile was seen for the second (average flux 560 kt day<sup>-1</sup>), suggesting that the first eruption was richer in SO<sub>2</sub>. This result is exemplified by plotting SO<sub>2</sub>  
20 flux against retrieved plume height above the vent, revealing distinct trends for the two events. We propose that a pre-erupted exsolved volatile phase was present prior to the first event, which could have led to the necessary overpressure to trigger the eruption. The second eruption, instead, was mainly driven by syneruptive degassing. This hypothesis is supported by melt inclusion measurements of sulfur concentrations in plagioclase phenocrysts and groundmass glass of tephra samples through electron microprobe analysis.

25 This work demonstrates that detailed interpretations of sub-surface magmatic processes during eruptions are possible using satellite SO<sub>2</sub> data. Quantitative comparisons of high temporal resolution plume height and SO<sub>2</sub> flux time-series offer a powerful tool to examine processes triggering and controlling eruptions. These novel tools open a new frontier in space-based volcanological research, and will be of great value when applied to remote, poorly monitored volcanoes, and to major eruptions that can have regional and global climate implications through, for example, influencing ozone depletion  
30 in the stratosphere and light scattering from stratospheric aerosols.



## 1 Introduction

Understanding the manner and the abundance of sulfur degassing from active volcanoes during explosive eruptions is one key to unravelling eruptive dynamics [Oppenheimer et al., 2011]. At a volcanic vent, sulfur gases contribute 2-35 vol% of total gas emissions, with SO<sub>2</sub> and H<sub>2</sub>S the dominant sulfur-bearing components, ranging between 1-25 vol% and 1-10 vol% respectively [Textor et al., 2004]. Satellite-based instruments operating in the ultraviolet and infrared have detected and quantified volcanic sulfur gases in the atmosphere since 1978 [Carn et al., 2016]. Nowadays, this is routinely done for SO<sub>2</sub> [Brenot et al., 2014], while few H<sub>2</sub>S satellite retrievals have been performed so far [Clarisse et al., 2011]. Satellite-based monitoring of volcanic SO<sub>2</sub> emissions is of value for poorly monitored volcanoes, which make up almost 95% of all volcanoes, but are also useful when well-monitored volcanoes erupt explosively, as local detection system can be saturated or blinded by ash.

Satellite images of volcanic SO<sub>2</sub> plumes contain a lot of information which can be extracted with the appropriate data analysis approach [McCormick et al., 2014; Hayer et al., 2016]. The most immediate information is typically vertical column amounts of SO<sub>2</sub> which can be readily used to determine a total SO<sub>2</sub> mass loading, and this is the most frequently used type of data provided in the literature. Valuable time-series information on SO<sub>2</sub> injection height and SO<sub>2</sub> flux time-series are also theoretically available, and these allow subtle observations and deductions on the volcanic processes driving eruptions, including the role of pre-eruptive gas accumulation [Westrich et al., 1992]. While a lot of work has been done on SO<sub>2</sub> satellite retrievals, a comprehensive, general methodology able to fully characterize both SO<sub>2</sub> flux and plume height time-series has not been successfully created to date. This is mainly due to the difficulty in retrieving SO<sub>2</sub> vertical profiles for individual SO<sub>2</sub> column amount pixels in an image. All satellite-based SO<sub>2</sub> column amount calculations are dependent on both the measured SO<sub>2</sub> optical depth and the plume height, and so quantification of SO<sub>2</sub> amounts requires accurate determination of plume height pixel by pixel in an image. Plume heights have been retrieved using infrared and ultraviolet spectra [Rix et al., 2012; Carboni et al., 2012; Grainger et al., 2016] and from numerical models applied to satellite images [Hughes et al., 2012; Clarisse et al., 2014; Pardini et al., 2017].

SO<sub>2</sub> flux time-series can be calculated from satellite imagery using a variety of methods (a review is presented in Theys et al., [2011]). Four methodologies have been applied: the box method [Lopez et al., 2013], the traverse method [Merucci et al., 2011], the delta method [Krueger et al., 1996] and inverse modelling [Eckhardt et al., 2008, Boichu et al., 2013]. Depending on the input parameters (plume age at the measurement time, satellite sensor spatial resolution, number of satellite acquisitions in a day, etc...) and expected outcomes (flux time-series, plume height time-series), each method has strengths and weakness. Box method is suitable for a first flux evaluation, but it needs constant wind speed and direction together with an *a-priori* estimation of plume height. The traverse method has been used to compare fluxes retrieved from satellite-based instruments with those from ground based measurements. This technique allows an almost real time estimate of SO<sub>2</sub> flux, despite it needs constant wind direction and plume height as input data. The box method is independent from wind speed and it produces an estimate of the SO<sub>2</sub> lifetime, however multiple satellite overpasses are needed. Finally, the



inverse modelling allows to compute fluxes at high temporal resolution even for plume presenting a complex vertical profile. The main drawback of this technique is the computational time.

In this work, we investigate SO<sub>2</sub> emissions during explosive eruptions with the aim of exhaustively examining the information which can be obtained from satellite imagery. We do this through application of a back-trajectory model to  
5 determine both the plume height for each SO<sub>2</sub> pixel in the satellite image, and the time at which each pixel's SO<sub>2</sub> was injected into the atmosphere. We adapted the Hybrid Single-Particle Lagrangian Integrated Trajectory model (HYSPLIT) [Stein et al., 2015] by integration with custom-built Python routines in order to create a semi-automated numerical procedure from which injection height and flux time-series are computed at high temporal resolution.

The algorithm we have implemented allow us to study both explosive and effusive eruptions, and, for each case study,  
10 specific input parameters (such as volcanic location, type of eruption, eruption time) can be set by the user. Our technique requires satellite and wind field datasets, which can derive from a variety of sources. Indeed, many satellite sensors can detect volcanic SO<sub>2</sub> atmospheric abundance [Carn et al., 2016], and, theoretically, each satellite dataset can be used as input for the model. The same can be done for the wind field data, which, however, has to be written in a format that HYSPLIT can read. Our algorithm is fast and it does not require constant wind speed or multiple satellite overpasses. The main  
15 advantage is the possibility to retrieve both SO<sub>2</sub> plume height and flux at high temporal and spatial resolution. However, results rely on the accuracy of wind field datasets, which could potentially affect the retrieved SO<sub>2</sub> abundances.

We applied our numerical method to GOME-2 satellite images of SO<sub>2</sub> plumes emitted by the two recent sub-Plinian eruptions occurred at Calbuco volcano, Chile, in April 2015. The eruptions have been classified as VEI 4 [Romero et al., 2016] and led to ozone depletion in Antarctica [Solomon et al., 2016, Ivy et al., 2017].

Our retrieved SO<sub>2</sub> injection height and flux time-series allow us to infer the presence of excess SO<sub>2</sub> at depth before the  
20 eruption. Furthermore, in order to validate and quantify the amount of excess SO<sub>2</sub>, we performed microprobe analysis of melt inclusions in plagioclase phenocrysts and ground mass of erupted products. This allows us to compare our numerical results with SO<sub>2</sub> loading derived from the “Petrological Method” [Devine et al., 1984], which uses information on the mass loading of each eruption and the volatile loss inferred from the difference in sulfur concentration between melt inclusion and  
25 groundmass.

## 2 Case study: the 22-23 April 2015 Calbuco eruptions

On the evening of 22 April 2015, Calbuco volcano started a new cycle of eruptive activity after 54 years of quiescence. Calbuco [41.33° S, 72.61° W] is an active stratovolcano located in the southern region of the Southern Volcanic Zone of the Andes, Chile. It has been volcanically active since the Late Pleistocene to the present, with the formation of 4 principle  
30 deposits. The last deposit has a “dome-cone” structure resulting from a series of recent major eruptions which occurred in 1912, 1961, 1971 and 1983-94 [Lopez-Escobar et al., 1992]. The new eruptive cycle started on 22 April 2015 and lasted 9 days, until 30 April 2015. An initial sub-Plinian eruption took place on the evening of 22 April (hereafter Eruption 1), and a second eruption occurred a few hours later in the morning of 23 April (hereafter Eruption 2).



Eruption 1 started suddenly at 20:54 UT. A volcanic column more than 15 km height rose from the main crater and tephra was dispersed in an East-Northeast direction. The overall duration of the event was 1.5 h. After Eruption 1 stopped, moderate seismic events in the form of volcanic tremor were recorded from 00:55 UT. At 04:00 UT, a new eruptive event (Eruption 2) occurred. The second eruption appeared to be more violent than the first one and lasted several hours. The eruptive column reached more than 15 km in altitude and tephra was dispersed in a North, Northeast and East direction. At 10:30 UT the eruption was declared over [SERNAGEOMIN, 2015a, 2015b, 2015c].

The eruptions are classified as VEI 4 [Romero et al., 2016] and they produced columns reaching the stratosphere. The stratospheric injection by the volcanic cloud together with the latitude of Calbuco, produced an impact on ozone recovery in Antarctica causing an increase in hole size of 4.4 million km<sup>2</sup> [Solomon et al., 2106; Ivy et al., 2017]. Moreover, extensive damage was caused to the Chilean economy, with agricultural and industrial resources close to Calbuco damaged by ash fall, and air traffic over Chile and Argentina disrupted for some hours [Romero et al., 2016].

Considering both the tephra fall and PDC deposits, the deposit volume estimated by Castruccio et al., [2016] is 0.38 km<sup>3</sup> (0.15 km<sup>3</sup> dense rock equivalent DRE assuming a deposit density 1000 kg m<sup>-3</sup>), while Romero et al., [2016] report a tephra fall deposit volume of 0.28 km<sup>3</sup> (0.11-0.13 km<sup>3</sup> DRE using a density of 2450 kg m<sup>-3</sup> for the 80% low density deposit and 2500 kg m<sup>-3</sup> for the remain 20%). These values are both within the 0.56±0.28 km<sup>3</sup> volume calculated by Van Eaton et al., [2016], which presents a DRE of 0.18±0.09 km<sup>3</sup> assuming a density of 2500 kg m<sup>-3</sup>.

### 3 Methods

The numerical procedure used here is a development of that presented by Pardini et al., [2017]. This new approach uses a two-step procedure based on a combination of forward and backward trajectories in order to decrease the uncertainties on the results arising from wind field errors. We also modified the post-processing phase, changing the selection criteria for acceptable trajectories and adding an SO<sub>2</sub> flux calculation. Due to the general implementation of the procedure, it can be easily applied to different volcanic systems to investigate SO<sub>2</sub> emissions during eruptive episodes or produced by quiescent degassing. In order to run the algorithm, two satellite images capturing the same volcanic plume at different times are required, as well as wind fields for each image. For each pixel of the computational domain in which SO<sub>2</sub> is detected, the method proposed here calculates three quantities. The first quantity,  $h$ , is the height at which the SO<sub>2</sub> is located at satellite measurement time instant (hereafter plume height). The second one,  $h_{vent}$ , is the height above volcanic vent at which SO<sub>2</sub> reaches the neutral buoyancy height and the prevailing atmospheric wind starts to disperse the gas into the atmosphere (hereafter injection height). The last one,  $t_{vent}$ , is the time when the SO<sub>2</sub> reaches the injection height (hereafter injection time). Knowing these three quantities and SO<sub>2</sub> column amount from satellite images, we are able to calculate the SO<sub>2</sub> mass loading of the plume and SO<sub>2</sub> flux time-series at a volcanic vent.

Plume parameters are computed by calculating trajectories run forwards and backwards in time. The trajectory calculation is performed by using HYSPLIT [Stein et al., 2015] with custom-designed routines written in the Python Programming Language.



The two-step procedure is done by using two satellite images collected at different times of a same volcanic SO<sub>2</sub> plume. The first image captures the SO<sub>2</sub> plume at day  $i$ , while the second image at day  $i + 1$ .

In Figure 1 we illustrate a schematic description of the technique used here. With the green pixels we indicate the region of the computational domain of the day  $i$  satellite image where SO<sub>2</sub> is detected, whilst with the yellow pixels we show the SO<sub>2</sub> plume captured at day  $i + 1$ . For each pixel  $j$  where SO<sub>2</sub> is detected and each plume heights  $h_j(i)$ , we calculate forward trajectories  $traj_j^f(i)$  up to the time of acquisition of the day  $i + 1$  image. Among these trajectories, only those consistent with the advected/dispersed plume at day  $i + 1$  are considered (for example, in Figure 1 only  $traj_j^f(1)$  and  $traj_j^f(3)$  are acceptable). Then, starting only from  $h_j(i)$  of each acceptable forward trajectory, we calculate backward trajectories  $traj_j^b(i)$ . We then select acceptable trajectories approaching volcanic vent location within a certain threshold distance (for example, in Figure 1 only  $traj_j^b(1)$  is acceptable). We adopt this two-step trajectory analysis to decrease the uncertainties on plume parameters due to wind field errors.

The definition of a threshold distance relies on physical constraints. Indeed, the distance of approach is set according to the growth of the umbrella cloud radius ( $r$ ) during the eruption. Thus, we consider acceptable a backward trajectory which minimal distance from the volcanic vent is less than  $r$ . Following Sparks et al., [1997], the radius of an umbrella cloud growing with time at the neutral buoyancy height can be expressed as:

$$r(t) = \left(\frac{3\lambda}{2\pi} N \cdot MER\right)^{\frac{1}{3}} t^{\frac{2}{3}}, \quad (1)$$

where  $\lambda$  is an empirical constant,  $N$  is the buoyancy frequency of the atmosphere and  $MER$  is the mass flow rate at buoyancy height. Following Sparks et al., [1997], we set  $\lambda$  equal to 0.8 and  $N$  equal to 0.17 for stratospheric strong plumes.

For each pixel  $j$  of the computational domain, and for each acceptable backward trajectory  $traj_j^b(i)$  starting from the pixel  $j$ , we extract the three plume parameters,  $h_j(i)$ ,  $h_{j_{vent}}(i)$  and  $t_{j_{vent}}(i)$ . The height  $h_j(i)$  is the altitude of the starting point of the backward trajectory  $traj_j^b(i)$  of the pixel  $j$ . Instead,  $h_{j_{vent}}(i)$  and  $t_{j_{vent}}(i)$  are respectively the height and the time at which each acceptable backward trajectory  $traj_j^b(i)$  approaches the vent. From the plume parameters calculated by our numerical method, we compute, for each pixel, the mean values ( $\bar{h}_j$ ,  $\bar{h}_{j_{vent}}$  and  $\bar{t}_{j_{vent}}$ ) and standard deviations ( $\sigma_{j_h}$ ,  $\sigma_{j_{h_{vent}}}$  and  $\sigma_{j_{t_{vent}}}$ ). Using these data, we can compute SO<sub>2</sub> mass loading in the volcanic plume and the mass of the tephra fall deposit. Finally, by associating pixels injection times ( $t_{j_{vent}}$ ) with their SO<sub>2</sub> mass loading, which is calculated from satellite SO<sub>2</sub> column amount, we calculate SO<sub>2</sub> flux time-series.

## 4 Results

### 4.1 Application of the numerical technique to Calbuco eruptions

To investigate SO<sub>2</sub> plumes emitted during the Calbuco eruptions we use satellite data from the GOME-2 sensor [Rix et al., 2008]. GOME-2 is an ultraviolet spectrometer (290-790 nm) aboard the polar-orbiting satellites MetOp-A (launched in



2006) and MetOp-B (launched in 2012) taking global measurements of atmospheric composition on daily basis. The two satellites operate in tandem with a temporal shift between acquisitions of 48 minutes and provide nadir-view scans with ground pixel size resolution equal to 40x40 km (swath of 960 km) in case of MetOp-A and 80x40 km (swath of 1920 km) in case of MetOp-B. One of the most sensitive parameters influencing SO<sub>2</sub> vertical column amount as retrieved from space is  
5 plume altitude at the satellite measurement time. This data is an input parameter for the retrieval algorithms leading to vertical column estimation; however, it cannot be easily *a-priori* assessed from space. In case of GOME-2, three vertical column densities are given for three hypothetical plume altitudes equal to 2.5 km, 6 km, 15 km.

The first GOME-2 image of the Calbuco SO<sub>2</sub> plume was collected at ~13:00 on 23 April 2015, after the end of the two eruptive events. Then, plumes advection/dispersion paths can be followed for about one month until they are diluted under  
10 the satellite detection limit (GOME-2 images can be displayed and datasets downloaded from the Support to Aviation Control Service (SACS) website <http://sacs.aeronomie.be/>). Due to GOME-2 MetOpA and B different pixel resolution, the original image is re-gridded into a new one presenting a spatial resolution of 30x30 km. In Figure 2(a) we report atmospheric SO<sub>2</sub> loading in Dobson Unit (DU) retrieved assuming the plume located at 2.5 km with a spatial resolution of 30x30 km. We used this dataset since, comparing it with the other retrievals (6 km and 15 km), we have an overestimation of the SO<sub>2</sub>  
15 atmospheric abundance and of its spatial distribution, ensuring, thus, that all the volcanic plume is considered in our model. In order to isolate volcanic plumes from background noise, we select pixels with a vertical column higher than a certain threshold (6 DU) calculated applied the Normalized Cloud-mass technique presented in Carn et al., [2008], see Figure 2(b). For our test case, the numerical wind data comes from the global ECMWF atmospheric reanalysis ERA Interim dataset with a 0.75° grid.

20 Since we do not make initial hypothesis on SO<sub>2</sub> plume altitude, and this information cannot be directly extrapolated from the satellite data, we initialize trajectories from 2 km (Calbuco altitude) to 30 km asl (upper stratosphere). Assuming an interval of 250 m between each starting height, we produce a total of 73 trajectories for each pixel. We set the centre position of each pixel as the starting point on the horizontal plane of each trajectory. The time at which the trajectories are initialized is coincident with the time at which the SO<sub>2</sub> vertical column was measured for each pixel.

25 After having reduced the number of possible trajectories going forward in time up to the time acquisition of the 24 April image, we accept backward trajectories approaching Calbuco vent location [41.33° S, 72.61° W] using Eq. (1). The umbrella cloud radius  $r(t)$  is evaluated every 10 min using the mass eruption rate ( $MER$ ) for both Eruption 1 and Eruption 2. Since we do not have a precise estimation of mass eruption rates, we perform a sensitivity analysis on  $MER$ , investigating the range  $[0.8 \cdot 10^6 \text{ kg s}^{-1} - 2.7 \cdot 10^7 \text{ kg s}^{-1}]$ . These values are chosen accordingly to the minimum and maximum  $MER$  calculated  
30 for the 2015 Calbuco eruptions by previous works [Romero et al., 2016, Castruccio et al., 2016, Van Eaton et al., 2016]. The sensitivity analysis is performed using the Design and Analysis toolKit for Optimization and Terascale (DAKOTA) [Adams et al., 2009], selecting a Latin Hypercube approach on a total number of 9 samples (i.e. 9 different values of  $MER$ ). Therefore, for each  $MER$  and for each of the two eruptions, the umbrella cloud radius grows from 0 km (beginning of the eruption) to a maximum value (ending of the eruption), which depends on the  $MER$ . However, numerical results show that



with the approaching condition expressed in Eq. (1) we do not have enough acceptable trajectories to cover most of the pixel in the computational domain. On the contrary, if we use a fixed maximum approaching distance for Eruption 1 and Eq. (1) for Eruption 2, our results can cover most of the volcanic cloud. This is due to several uncertainties given by wind data, trajectory calculation and SO<sub>2</sub> spatial distribution captured by the satellite. Since our aim is to provide a good estimation of the SO<sub>2</sub> mass loading in the volcanic cloud, we prefer to consider a solution which cover most of the pixels in the computational domain. For this reason, for Eruption 1, we use a maximum approaching radius  $r = 280$  km, whilst for Eruption 2 we calculate  $r(t)$  every 10 minutes using Eq. (1). The maximum values for the umbrella radius computed at the end of Eruption 2 are 150 and 360 km for the two *MER* end members (respectively  $0.8 \cdot 10^6$  kg s<sup>-1</sup> and  $2.7 \cdot 10^7$  kg s<sup>-1</sup>). The sensitivity analysis performed on *MER* produces 9 sets of acceptable trajectories for each pixel (one set for each *MER*). For a given *MER*, the number of the acceptable trajectories can vary from 0 (i.e. no acceptable trajectories starting from the considered pixel) to 73 (i.e. all the trajectories starting from the considered pixel are acceptable).

## 4.2 Numerical results

Using the previously described technique, we calculate the plume height, the injection height and the injection time for each pixel of the computational domain where SO<sub>2</sub> is detected. Figures 3 and 4 report both the mean values ( $\bar{h}$ ,  $\bar{h}_{vent}$  and  $\bar{t}_{vent}$ ) and standard deviations ( $\sigma_h$ ,  $\sigma_{h_{vent}}$  and  $\sigma_{t_{vent}}$ ) of plume parameters calculated for each pixel. Figure 3 shows the SO<sub>2</sub> cloud emitted from Eruption 1, whilst in Figure 4 we plot the one emitted from Eruption 2. We do not separate *a-priori* the plume of Eruption 1 from the one of Eruption 2, but it is the model that, according to the approaching time and radius, distinguishes the two plumes. Figures 3(a), (d) and 4(a), (d) show respectively  $\bar{h}$  and  $\sigma_h$  computed for each pixel of the computational domain. Similarly, Figures 3(b), (e) and 4(b), (e) report  $\bar{h}_{vent}$  and  $\sigma_{h_{vent}}$  respectively, whereas Figures 3(c), (f) and 4(c), (f) illustrate  $\bar{t}_{vent}$  and  $\sigma_{t_{vent}}$ .

As we can see from Figure 3 and 4, the whole SO<sub>2</sub> plume is split into two multi-layered clouds, both transported in the same direction (North North-East). The SO<sub>2</sub> injected into the atmosphere at the beginning of the eruptive phases travelled furthest from the vent, while pixels closer to vent location contain SO<sub>2</sub> emitted at the end of the two eruptions.

Due to low vertical velocity at stratospheric heights,  $\bar{h}$  and  $\bar{h}_{vent}$  are almost coincident (Figure 3(a), (b) and 4(a), (b)) and similar result is obtained for  $\sigma_{h_{vent}}$  and  $\sigma_h$  (Figure 3(d), (e) and 4(d), (e)). SO<sub>2</sub> injected at the highest altitudes during Eruption 1 (from ~15 to 22 km) has been transported North-East, while SO<sub>2</sub> injected at lower altitudes (from ~11 to 15 km) has been mainly drifted North and it composes the tail of the plume. Moreover, a lower layer, below ~10 km, can be observed for cloud related to Eruption 1. On the contrary, SO<sub>2</sub> plume emitted during Eruption 2 (Figure 4) presents a more compact shape than the one of Eruption 1. A mean height of ~14 km both at vent and at satellite overpass is computed, with peaks of ~18 km (Figure 4(a), (b)). For almost the whole cloud of Eruption 1,  $\sigma_h$  and  $\sigma_{h_{vent}}$  are ~0.5 km (Figure 3(d), (e)), whilst for Eruption 2 are in the range 0-6 km with a mean value of 2 km (Figure 4(d), (e)). Finally, uncertainties on injection time are 17 min and 45 min for Eruption 1 and Eruption 2 respectively (Figures 3(f) and 4(f)).



Our height retrievals appear to be consistent with those derived from analysis of both the tephra deposit and remote sensing techniques. Following the method of maximum clast diameters [Carey and Sparks, 1986], Romero et al., [2016] computed maximum column heights of  $15.4 \pm 3.08$  km during Eruption 1 and the first phase of Eruption 2, while a decrease during the last phase of Eruption 2 emerges with heights of 12-13 km. Similar values are reported by Castruccio et al., [2016] with the only difference of proposing an increase in column height at the end the Eruption 2.

These values are also in agreement with what presented by Van Eaton et al., [2016] considering the growth of the umbrella cloud (14.5-15.5 km for Eruption 1 and 16.9-17.3 km for Eruption 2). The main difference we notice from these deposits estimates of plume height compared to those performed by our numerical simulation is the absence of heights higher than 20 km. However, Vidal et al., [2017] show, using a dual polarized weather radar, the main column located between 7 and 15 km for Eruption 2, with a maximum value of  $\sim 23$  km asl, in agreement with our estimations for plume heights.

In Figure 5(a) we plot in red the pixels from which we have at least one acceptable trajectory for all the *MER* investigated, whilst in grey the pixels of the computational domain at satellite measurement time on 23 April 2015. As we can see, our numerical results cover most of the computational domain, even though we do not find any acceptable trajectory for the sparse pixels located in the northern region. From Figure 2(b) we can observe that the  $\text{SO}_2$  column amount for these pixels is near to the chosen threshold, and their location is far from the main plume. Combining this information with our numerical results, we can conclude that  $\text{SO}_2$  amount in these pixels is more likely to be associated with background noise rather than volcanic  $\text{SO}_2$  emissions. In order to check the consistency of our numerical results, we perform a 24 h forward trajectory simulation initializing trajectories from the altitudes  $h_j(i)$  from which we have found acceptable backward trajectories on the 23 April image. Figure 5(d) shows the comparison of our 24 h forward trajectory simulation with the volcanic  $\text{SO}_2$  cloud taken from the 24 April satellite image (considering pixels with a vertical column higher than 6 DU), and a good match with the original image can be observed.

#### 4.2.1 Masses estimation from numerical results and $\text{SO}_2$ flux time-series

$\text{SO}_2$  vertical columns retrieved from satellite data depend on several factors, such as plume height,  $\text{SO}_2$  lifetime and satellite sensors signal saturation.  $\text{SO}_2$  retrievals from GOME-2 report vertical columns for each pixel at 3 hypothetical plume heights of 2.5 km, 6 km, 15 km (Figure 6(a)-(c)). We interpolate  $\text{SO}_2$  column amount between these three points and use our calculated mean  $\text{SO}_2$  height ( $\bar{h}$ ) to correct the column amount. In our test case, the effect related to  $\text{SO}_2$  lifetime can be neglected. Indeed, lifetime of volcanic  $\text{SO}_2$  injected into the stratosphere depends primarily on injection altitude, and can vary from 8-9 days for 11 km height plumes [Krotkov et al., 2010] to 25 days for higher injection altitudes [Guo et al., 2004]. The brief time ( $<16$  hours) between eruptions and satellite measurement means that  $\text{SO}_2$  losses due to deposition or chemical conversion are not significant. Furthermore, we correct possible 30% underestimations of  $\text{SO}_2$  loading due to signal saturation for vertical columns higher than 50-100 DU [Rix et al., 2008]. Combining all of this information, we produce a corrected  $\text{SO}_2$  column amount image for 2015 Calbuco eruptions (Figure 6(d)).



Comparing our height-corrected SO<sub>2</sub> column amounts with those retrieved from GOME-2, we see good agreement with satellite data between 6 km and 15 km. Mean square root errors computed from our numerical results and GOME-2 retrievals, reveal that the *a-priori* image which agrees best with our height-corrected SO<sub>2</sub> atmospheric loading is that assuming 15 km height. Mean square root errors are equal to 45.05 DU for the 2.5 km map, 12.51 DU and 8.75 DU for the 6 km and 15 km maps respectively.

We use the corrected SO<sub>2</sub> column amount to determine a total SO<sub>2</sub> mass loading of 300±46 kt of SO<sub>2</sub> for the overall Calbuco eruptions, with 160±30 kt produced by Eruption 1 and 140±35 kt by Eruption 2. For each pixel of the computational domain we plot the retrieved SO<sub>2</sub> loading [kt] in Figure 7(a), (b). With contours we indicate mean altitudes at which SO<sub>2</sub> is located at satellite measurement time. During Eruption 1 the bulk of the SO<sub>2</sub> (83% of the total) was injected into the atmosphere in the range 8-16 km, while the remaining 17% was injected at heights ranging from 17-21 km (Figure 7(a)). On the contrary, Eruption 2 was characterized with 55% of the SO<sub>2</sub> injected at 15 km, 41% at 13 km and 4% at 3 km (Figure 7(b)).

Our retrieval of plume height time-series opens the possibility of quantifying mass eruption rate time-series, and to compare these data with field data. For the Calbuco eruptions, separation of volcanic ash and SO<sub>2</sub> gas has not been observed, so retrieved SO<sub>2</sub> injection heights are representative of column height evolution during the eruptions. Column height is primary controlled by the thermal buoyancy of the erupted material, which is a function of the mass flux supplied during the eruption [Sparks et al., 1997]. We use our mean injection height time-series to calculate mass eruption rate (*MER*) every 10 minutes during the eruptions and we compute masses of erupted solid material by integrating *MER* over time. We infer 9·10<sup>4</sup> kt emitted during Eruption 1 and 25·10<sup>4</sup> kt during Eruption 2. These values are in good agreement with those from Castruccio et al., [2016] which report 8·10<sup>4</sup> kt for Eruption 1 and 32·10<sup>4</sup> kt for Eruption 2. Our satellite-based interpretation seems to confirm the eruptive scenario proposed by Castruccio et al., [2016] which assign the first or the four layers of the deposit to the first eruption and the other three to the second one. Differently, Romero et al., [2016] assign the first two layers to Eruption 1 and the other two to Eruption 2, despite the two authors agree on the general stratigraphy.

With density of ~2500 kg m<sup>-3</sup> for the whole deposit, we compute a deposit dense rock equivalent (DRE) of 0.136 km<sup>3</sup>, with 0.036 km<sup>3</sup> resulting from Eruption 1 and 0.1 km<sup>3</sup> from Eruption 2. For Eruption 1 a magma volume of 0.036 km<sup>3</sup> produced 0.16 Mt of SO<sub>2</sub>, while 0.1 km<sup>3</sup> of magma produced 0.14 Mt of SO<sub>2</sub> for Eruption 2. Thus, Eruption 1 produced about one order of magnitude excess SO<sub>2</sub> per unit mass erupted than Eruption 2.

Finally, by associating the injection time at the vent ( $t_{vent}$ ) for each pixel SO<sub>2</sub> mass loading we calculate SO<sub>2</sub> flux time-series (Figure 8(a)). The similar amount of SO<sub>2</sub> released during the two eruptions and the different duration of the events (1.5 h and 6 h) are reflected in the average SO<sub>2</sub> fluxes. Eruption 1 produced an intense gas emission with mean flux of 2560 kt day<sup>-1</sup>, while a smoother Gaussian shape curve can be observed for Eruption 2 together with a much lower mean flux of 560 kt day<sup>-1</sup>. SO<sub>2</sub> flux is well-correlated with mean injection heights for both eruptions (Figure 8(b)). Comparing SO<sub>2</sub> flux and injection height time-series, two different volcanic processes driving Eruption 1 and 2 emerge. This is reflected in the similar total amount of SO<sub>2</sub> (~150 kt) released in different time scale (1.5 h and 6 h) but in a similar range of altitudes (13-15 km).



## 5. Discussion

We found that the SO<sub>2</sub> emitted per km<sup>3</sup> of erupted lavas during Eruption 1 was about one order of magnitude higher than that of Eruption 2, and this indicates a role for excess SO<sub>2</sub> in Eruption 1. Excess SO<sub>2</sub> has been invoked to explain a large body of evidence where satellite detection of volcanic SO<sub>2</sub> plumes demonstrated that the amount of SO<sub>2</sub> released into the atmosphere during volcanic eruptions, both explosive and effusive, can exceed that resulting from syneruptive volatile exsolution [Devine et al., 1984]. Wallace [2001] shows that there is a fixed ratio between the volume of erupted magma (expressed in km<sup>3</sup>) and the SO<sub>2</sub> loading (expressed in Mt) which is released due to syneruptive degassing of erupted magma. In particular, for an andesite magma, the ratio between these two quantities is typically ~1 Mt km<sup>-3</sup>. However, in some cases, the SO<sub>2</sub> emitted is higher than that which can be produced by syneruptive degassing. This means that the SO<sub>2</sub> released into the atmosphere during an eruption is the sum of two contributions. The first is the SO<sub>2</sub> derived from syneruptive degassing of erupted magma, while the second is the SO<sub>2</sub> derived from a pre-existing exsolved gas phase present inside the magma chamber before the eruption starts. The process which produces such excess SO<sub>2</sub> depend on tectonic setting, magma type, magma evolution and eruption style [Shinohara 2008]. However, excess SO<sub>2</sub> appears to be particularly characteristic of explosive eruptions of intermediate and silicic magma in subduction zone settings [Andres et al., 1991], such as Calbuco. Romero et al., [2016] show that the 2015 Calbuco eruptions were fed by a basaltic-andesitic magma (~55 wt.% of SiO<sub>2</sub>), and therefore the ratio between the SO<sub>2</sub> emitted and the volume of magma erupted might be expected to be close to ~1 Mt km<sup>-3</sup>. Our results for Eruption 2 are consistent with the relation showed by Wallace [2001]. However, for Eruption 1, the ratio between the SO<sub>2</sub> released and the volume ejected is ~5 Mt km<sup>-3</sup>. This clearly suggests that, prior to Eruption 1, there was already an exsolved volatile phase in the magma chamber.

For sub-Plinian eruptions like Calbuco 2015 the most likely mechanism responsible for excess SO<sub>2</sub> is pre-eruptive exsolution of volatiles supplied from deeper magma [Wallace 2001; Shinohara 2008]. Due to buoyancy forces, bubbles migrated at the top of the magma chamber, forming a gas-rich cupola. We suggest that the overpressure resulting from this deep exsolution may have also provided the trigger for the eruption onset. During the course of Eruption 1, all the pre-existing volatile phase was ejected into the atmosphere. However, the short repose time between the two eruptions was not enough to accumulate significant amounts of gas from deeper magma. Thus, we can infer that Eruption 2 was driven mainly by syneruptive volatile exsolution without the presence of a volatile excess from depth.

In order to test this hypothesis of a pre-accumulated gas phase powering Eruption 1, and a simple syneruptive magma ascent sustaining Eruption 2, we performed electron microprobe analyses (technical details are reported in the Supplementary Materials) on the erupted products of both eruptions, to derive SO<sub>2</sub> mass loss in both eruptions. In detail, the scoriae erupted from Calbuco contain plagioclase, orthopyroxene and clinopyroxene as phenocrysts and a crystallised groundmass with patches of glass. Melt inclusions (MIs) are hosted in plagioclase phenocrysts and they are characterized by spherical to oblate shape. Sizes of MIs range from 30 to 300 μm. The groundmass is composed of glass patches with variable microlite contents ranging from lowly to heavily crystallized groundmass. The composition of MIs is andesitic, instead the



groundmass glass composition is andesitic-dacitic (see Supplementary Materials). According to electron microprobe analyses, differences between sulfur contents of glassy melt inclusions ( $S_{MI}$ ) and matrix glasses ( $S_{gm}$ ) scaled to masses of erupted solid material provide estimates of minimum sulfur yield to the atmosphere during an eruption. In order to compare our satellite estimates of  $SO_2$  mass loadings with elemental sulfur concentrations measured from microprobe analyses, it is useful to convert sulfur mass loadings into  $SO_2$  mass loadings, which is readily achieved by multiplying by two, following the molecular weight of  $SO_2$  ( $64 \text{ g mol}^{-1}$ ) and atomic weight of sulfur ( $32 \text{ g mol}^{-1}$ ), see  $m(SO_2)_{PETR}$  column in Table 1. From the petrological method we infer  $38 \pm 12$  kt and  $120 \pm 26$  kt of  $SO_2$  emitted during Eruption 1 and 2 respectively. Comparing masses of  $SO_2$  derived from our numerical satellite-based technique, with those resulting from microprobe analyses, we calculate the excess  $SO_2$  [Devine et al., 1984]. For Eruption 1, we found  $122 \pm 28$  kt of excess  $SO_2$ , whereas for Eruption 2 just  $20 \pm 38$  kt, see  $m(SO_2)_{ex}$  of Table 1. This demonstrates that about the 76% of the  $SO_2$  emitted during Eruption 1 was already present as part of the pre-eruptive exsolved gas phase, in agreement with our hypothesis. Instead, for Eruption 2 there is, within error limits, no excess  $SO_2$ .

## 6 Conclusions

We have developed a new technique to retrieve  $SO_2$  flux time-series and eruption plume height at high spatial (30 km) and time resolution (10 minutes). Our numerical procedure, which combines satellite imagery of volcanic  $SO_2$  plumes with forward and backward trajectory simulations, can be generally applied, and used to investigate  $SO_2$  emission during any type of volcanic eruption. The algorithm is computationally efficient, and can be run in an automated manner on a standard PC in <12 hours. Retrieved plume heights are used to correct the assumption that the whole plume is located at the same hypothetical altitude, thus producing corrected  $SO_2$  columnar amount maps.

Here, we quantified  $SO_2$  emissions from the recent April 2015 Calbuco eruptions using imagery from the GOME-2 satellite sensor. We retrieved both  $SO_2$  injection height and flux time-series and used them to unravel triggering mechanisms and volcanic processes of the Calbuco eruption. We found excellent agreement between the integrated mass eruption rates inferred from plume height time-series and field studies of the eruption deposit masses. Furthermore, our results highlight the presence of different exsolved volatile phase at depth between the two eruptions. Thanks to the quantitative comparison of  $SO_2$  flux and plume height time-series, we infer the presence of excess  $SO_2$  in Eruption 1. We found that at least 76% of total  $SO_2$  emitted in Eruption 1 was sourced from pre-eruptive volatile exsolution. We suggest that bubbles migrated to the top of the magma chamber forming a gas-rich cupola. The overpressure caused by this gas accumulation could have played a key role in triggering Eruption 1. On the other hand, Eruption 2 was consistent with a syneruptive degassing, since no excess  $SO_2$  was observed. Electron microprobe analyses performed on Calbuco samples confirmed our conclusions, validating our hypothesis made just from our numerical technique.

This work highlights the capability of trajectory analysis of satellite  $SO_2$  imagery to extract  $SO_2$  height and flux time-series and reveal sub-surface magmatic processes. We highlight that plotting time-series of retrieved  $SO_2$  flux against retrieved plume heights is an effective tool to examine patterns in eruption processes, the role of excess  $SO_2$  degassing, and compare



eruptions. Our approach could be applied to the reanalysis of SO<sub>2</sub> imagery collected during past volcanic eruptions. This opens the possibility of a database that would be a powerful tool for real time analysis of satellite data collected during an eruption. Indeed, satellite images of volcanic SO<sub>2</sub> plumes are available in almost real time when an eruption occurs and they could be used not only for aviation safety mitigation but also for operational monitoring of subsurface processes especially in conjunction with other geophysical data. These data may greatly help the quantification of stratospheric mass loadings of SO<sub>2</sub>, which can impact global temperatures through the formation of sulphuric acid aerosols [Kirchner et al., 1999], and mass loadings of HCl, using either assumptions or measurements of SO<sub>2</sub>/HCl masses, and these could be invaluable in the determination of ozone depletion processes [Solomon et al., 2016; Ivy et al., 2017].

## 10 References

Adams, B. M., Bohnhoff, W. J., Dalbey, K. R., Eddy, J. P., Eldred, M. S., Gay, D. M., Haskell, K., Hough, P. D. and Swiler, L. P.: DAKOTA, a multilevel parallel object-oriented framework for design optimization, parameter estimation, uncertainty quantification, and sensitivity analysis: version 5.0 user's manual, Sandia National Laboratories, Tech. Rep. SAND2010-2183, doi:DOI: 10.2172/991842, 2009.

Boichu, M., Menut, L., Khvorostyanov, D., Clarisse, L., Clerbaux, C., Turquety, S. and Coheur, P.-F.: Inverting for volcanic SO<sub>2</sub> flux at high temporal resolution using spaceborne plume imagery and chemistry-transport modelling: the 2010 Eyjafjallajökull eruption case-study, *Atmospheric Chemistry and Physics*, 13(17), 8569–8584, doi:10.5194/acp-13-8569-2013, 2013.

Brenot, H., Theys, N., Clarisse, L., Van Geffen, J., Van Gent, J., Van Roozendaal, M., Van Der A, R., Hurtmans, D., Coheur, P.-F. and Clerbaux, C.: Support to Aviation Control Service (SACS): an online service for near real-time satellite monitoring of volcanic plumes, *Natural hazards and earth system sciences*, 14(5), 1099–1123, doi:10.5194/nhess-14-1099-2014, 2014.

Carboni, E., Grainger, R., Walker, J., Dudhia, A. and Siddans, R.: A new scheme for sulphur dioxide retrieval from IASI measurements: application to the Eyjafjallajökull eruption of April and May 2010, *Atmospheric Chemistry and Physics*, 12(23), 11417–11434, doi:doi:10.5194/acp-12-11417-2012, 2012.

Carey, S. and Sparks, R. S. J.: Quantitative models of the fallout and dispersal of tephra from volcanic eruption columns, *Bulletin of Volcanology*, 48(2), 109–125, doi:10.1007/BF01046546, 1986.

Carn, S. A., Krueger, A. J., Arellano, S., Krotkov, N. A. and Yang, K.: Daily monitoring of Ecuadorian volcanic degassing from space, *Journal of Volcanology and Geothermal Research*, 176(1), 141–150, doi:10.1016/j.jvolgeores.2008.01.029, 2008.



- Carn, S. A., Clarisse, L., and Prata, A. J.: Multi-decadal satellite measurements of global volcanic degassing, *Journal of Volcanology and Geothermal Research*, 311, 99-134, [10.1016/j.jvolgeores.2016.01.002](https://doi.org/10.1016/j.jvolgeores.2016.01.002), 2016.
- Castruccio, A., Clavero, J., Segura, A., Samaniego, P., Roche, O., Le Pennec, J.-L. and Droguett, B.: Eruptive parameters and dynamics of the April 2015 sub-Plinian eruptions of Calbuco volcano (southern Chile), *Bulletin of Volcanology*, 78(9), 62, [doi:10.1007/s00445-016-1058-8](https://doi.org/10.1007/s00445-016-1058-8), 2016.
- Clarisse, L., Coheur, P.-F., Chefdeville, S., Lacour, J.-L., Hurtmans, D. and Clerbaux, C.: Infrared satellite observations of hydrogen sulfide in the volcanic plume of the August 2008 Kasatochi eruption, *Geophysical research letters*, 38(10), [doi:10.1029/2011GL047402](https://doi.org/10.1029/2011GL047402), 2011.
- 10 Clarisse, L., Coheur, P.-F., Theys, N., Hurtmans, D. and Clerbaux, C.: The 2011 Nabro eruption, a SO<sub>2</sub> plume height analysis using IASI measurements, *Atmospheric chemistry and physics*, 14(6), 3095–3111, [doi:10.5194/acp-14-3095-2014](https://doi.org/10.5194/acp-14-3095-2014), 2014.
- Devine, J. D., Sigurdsson, H., Davis, A. N. and Self, S.: Estimates of sulfur and chlorine yield to the atmosphere from volcanic eruptions and potential climatic effects, *Journal of Geophysical Research: Solid Earth*, 89(B7), 6309–6325, [doi:10.1029/JB089iB07p06309](https://doi.org/10.1029/JB089iB07p06309), 1984.
- 15 Eckhardt, S., Prata, A. J., Seibert, P., Stebel, K. and Stohl, A.: Estimation of the vertical profile of sulfur dioxide injection into the atmosphere by a volcanic eruption using satellite column measurements and inverse transport modeling, *Atmospheric Chemistry and Physics*, 8(14), 3881–3897, [doi:10.5194/acp-8-3881-2008](https://doi.org/10.5194/acp-8-3881-2008), 2008.
- Grainger, R. G., Mather, T. A., Pyle, D. M., Thomas, G. E., Smith, A. J. and Koukouli, M. E.: The vertical distribution of volcanic SO<sub>2</sub> plumes measured by IASI, *Atmospheric Chemistry and Physics*, 16(7), 4343, [doi:10.5194/acp-16-4343-2016](https://doi.org/10.5194/acp-16-4343-2016),  
20 2016.
- Guo, S., Bluth, G. J., Rose, W. I., Watson, I. M. and Prata, A. J.: Re-evaluation of SO<sub>2</sub> release of the 15 June 1991 Pinatubo eruption using ultraviolet and infrared satellite sensors, *Geochemistry, Geophysics, Geosystems*, 5(4), [doi:10.1029/2003GC000654](https://doi.org/10.1029/2003GC000654), 2004.
- Hayer, C. S., Wadge, G., Edmonds, M. and Christopher, T.: Sensitivity of OMI SO<sub>2</sub> measurements to variable eruptive  
25 behaviour at Soufrière Hills Volcano, Montserrat, *Journal of Volcanology and Geothermal Research*, 312, 1–10, [doi:10.1016/j.jvolgeores.2016.01.014](https://doi.org/10.1016/j.jvolgeores.2016.01.014), 2016.
- Hughes, E. J., Sparling, L. C., Carn, S. A. and Krueger, A. J.: Using horizontal transport characteristics to infer an emission height time series of volcanic SO<sub>2</sub>, *Journal of Geophysical Research: Atmospheres*, 117(D18), [doi:10.1029/2012JD017957](https://doi.org/10.1029/2012JD017957),



- 2012.
- Ivy, D. J., Solomon, S., Kinnison, D., Mills, M. J., Schmidt, A. and Neely, R. R.: The influence of the Calbuco eruption on the 2015 Antarctic ozone hole in a fully coupled chemistry-climate model, *Geophysical Research Letters*, 44(5), 2556–2561, doi:10.1002/2016GL071925, 2017.
- 5 Kirchner, I., G. Stenchikov, H.-F. Graf, A. Robock. J. Antuna, Climate model simulation of winter warming and summer cooling following the 1991 Mount Pinatubo volcanic eruption, *J. Geophys. Res.*, 104, 19,039-19,055, 1999.
- Krotkov, N. A., Schoeberl, M. R., Morris, G. A., Carn, S. and Yang, K.: Dispersion and lifetime of the SO<sub>2</sub> cloud from the August 2008 Kasatochi eruption, *Journal of Geophysical Research: Atmospheres*, 115(D2), doi:10.1029/2010JD013984, 2010.
- 10 Krueger, A. J., Schnetzler, C. C. and Walter, L. S.: The December 1981 eruption of Nyamuragira volcano (Zaire), and the origin of the “mystery cloud” of early 1982, *Journal of Geophysical Research: Atmospheres*, 101(D10), 15191–15196, doi:10.1029/96JD00221, 1996.
- Lopez, T., Carn, S., Werner, C., Fee, D., Kelly, P., Doukas, M., Pfeffer, M., Webley, P., Cahill, C. and Schneider, D.: Evaluation of Redoubt Volcano’s sulfur dioxide emissions by the Ozone Monitoring Instrument, *Journal of Volcanology and*
- 15 *Geothermal Research*, 259, 290–307, doi:10.1016/j.jvolgeores.2012.03.002, 2013.
- Lopez-Escobar, L., Parada, M. A., Moreno, H., Frey, F. A. and Hickey-Vargas, R. L.: A contribution to the petrogenesis of Osomo and Calbuco volcanoes, Southern Andes (41° 00’-41° 30’S): comparative study, *Andean Geology*, 19(2), 211–226, doi:<http://dx.doi.org/10.5027/andgeoV19n2-a05>, 1992.
- McCormick, B. T., Herzog, M., Yang, J., Edmonds, M., Mather, T. A., Carn, S. A., Hidalgo, S. and Langmann, B.: A
- 20 comparison of satellite-and ground-based measurements of SO<sub>2</sub> emissions from Tungurahua volcano, Ecuador, *Journal of Geophysical Research: Atmospheres*, 119(7), 4264–4285, doi:10.1002/2013JD019771, 2014.
- Merucci, L., Burton, M., Corradini, S. and Salerno, G. G.: Reconstruction of SO<sub>2</sub> flux emission chronology from space-based measurements, *Journal of Volcanology and Geothermal Research*, 206(3), 80–87, doi:10.1016/j.jvolgeores.2011.07.002, 2011.
- 25 Oppenheimer, C., Scaillet, B. and Martin, R. S.: Sulfur degassing from volcanoes: source conditions, surveillance, plume chemistry and earth system impacts, *Reviews in Mineralogy and Geochemistry*, 73(1), 363–421, doi:10.2138/rmg.2011.73.13, 2011.



- Pardini, F., Burton, M., Vitturi, M. de' Michieli, Corradini, S., Salerno, G., Merucci, L. and Di Grazia, G.: Retrieval and intercomparison of volcanic SO<sub>2</sub> injection height and eruption time from satellite maps and ground-based observations, *Journal of Volcanology and Geothermal Research*, 331, 79–91, doi:10.1016/j.jvolgeores.2016.12.008, 2017.
- Rix, M., Valks, P., Hao, N., Erbertseder, T. and Van Geffen, J.: Monitoring of volcanic SO<sub>2</sub> emissions using the GOME-2 satellite instrument, in *Use of Remote Sensing Techniques for Monitoring Volcanoes and Seismogenic Areas, 2008. USEReST 2008. Second Workshop on*, pp. 1–5, IEEE., 2008.
- Rix, M., Valks, P., Hao, N., Loyola, D., Schlager, H., Huntrieser, H., Flemming, J., Koehler, U., Schumann, U. and Inness, A.: Volcanic SO<sub>2</sub>, BrO and plume height estimations using GOME-2 satellite measurements during the eruption of Eyjafjallajökull in May 2010, *Journal of Geophysical Research: Atmospheres*, 117(D20), doi:10.1029/2011JD016718, 2012.
- 10 Romero, J. E., Morgavi, D., Arzilli, F., Daga, R., Caselli, A., Reckziegel, F., Viramonte, J., Díaz-Alvarado, J., Polacci, M. and Burton, M.: Eruption dynamics of the 22–23 April 2015 Calbuco volcano (Southern Chile): Analyses of tephra fall deposits, *Journal of Volcanology and Geothermal Research*, 317, 15–29, doi:10.1016/j.jvolgeores.2016.02.027, 2016.
- SERNAGEOMIN, 2015a. Reporte Especial de Actividad Volcánica (REAV) Región de los Lagos. (REAV) Año 2015 Abril 22 (20:45 HL).
- 15 SERNAGEOMIN, 2015b. Reporte Especial de Actividad Volcánica (REAV) Región de los Lagos. Año 2015 Abril 22 (22:30 HL).
- SERNAGEOMIN, 2015c. Reporte Especial de Actividad Volcánica (REAV) Región de los Lagos. Año 2015 Abril 23 (10:30 HL)
- Shinohara, H.: Excess degassing from volcanoes and its role on eruptive and intrusive activity, *Reviews of Geophysics*, 20 46(4), doi:10.1029/2007RG000244, 2008.
- Solomon, S., Ivy, D.J., Kinnison, D., Mills, M.J., Neely, R.R. and Schmidt, A. Emergence of healing in the Antarctic ozone layer. *Science*, 353(6296), pp.269-274, 2016.
- Sparks, R. S. J.: M. I. Bursik, SN Carey, JS Gilbert, LS Glaze, H. Sigurdsson and AW Woods. *Volcanic Plumes*, Wiley: New York., 1997.
- 25 Stein, A. F., Draxler, R. R., Rolph, G. D., Stunder, B. J., Cohen, M. D. and Ngan, F.: NOAA's HYSPLIT atmospheric transport and dispersion modeling system, *Bulletin of the American Meteorological Society*, 96(12), 2059–2077, doi:10.1175/BAMS-D-14-00110.1, 2015.



- Textor, C., Graf, H.-F., Timmreck, C. and Robock, A.: Emissions from volcanoes, in Emissions of Atmospheric Trace Compounds, pp. 269–303, Springer., 2004.
- Theys, N., Campion, R., Clarisse, L., van Gent, J., Dils, B., Corradini, S., Merucci, L., Coheur, P. F., Van Roozendael, M. and Hurtmans, D.: Volcanic SO<sub>2</sub> fluxes derived from satellite data: a survey using OMI, GOME-2, IASI and MODIS, 5 Atmospheric Chemistry and Physics (ACP), doi:10.5194/acp-13-5945-2013, 2013.
- Van Eaton, A. R., Amigo, Á., Bertin, D., Mastin, L. G., Giacosa, R. E., González, J., Valderrama, O., Fontijn, K. and Behnke, S. A.: Volcanic lightning and plume behavior reveal evolving hazards during the April 2015 eruption of Calbuco volcano, Chile, Geophysical Research Letters, 43(7), 3563–3571, doi:10.1002/2016GL068076, 2016.
- Vidal, L., Nesbitt, S. W., Salio, P., Farias, C., Nicora, M. G., Osoreo, M. S., Mereu, L. and Marzano, F. S.: C-band Dual-10 Polarization Radar Observations of a Massive Volcanic Eruption in South America, IEEE Journal of Selected Topics in Applied Earth Observations and Remote Sensing, 10(3), 960–974, doi:DOI: 10.1109/JSTARS.2016.2640227, 2017.
- Wallace, P. J.: Volcanic SO<sub>2</sub> emissions and the abundance and distribution of exsolved gas in magma bodies, Journal of Volcanology and Geothermal Research, 108(1), 85–106, doi:10.1016/S0377-0273(00)00279-1, 2001.
- Westrich, H. R. and Gerlach, T. M.: Magmatic gas source for the stratospheric SO<sub>2</sub> cloud from the June 15, 1991, eruption of 15 Mount Pinatubo, Geology, 20(10), 867–870, doi:10.1130/0091-7613(1992)020<0867:MGSFTS>2.3., 1992.
- Wilson, L., Sparks, R. S. J. and Walker, G. P.: Explosive volcanic eruptions—IV. The control of magma properties and conduit geometry on eruption column behaviour, Geophysical Journal International, 63(1), 117–148, doi:10.1111/j.1365-246X.1980.tb02613.x, 1980.

### Acknowledgements

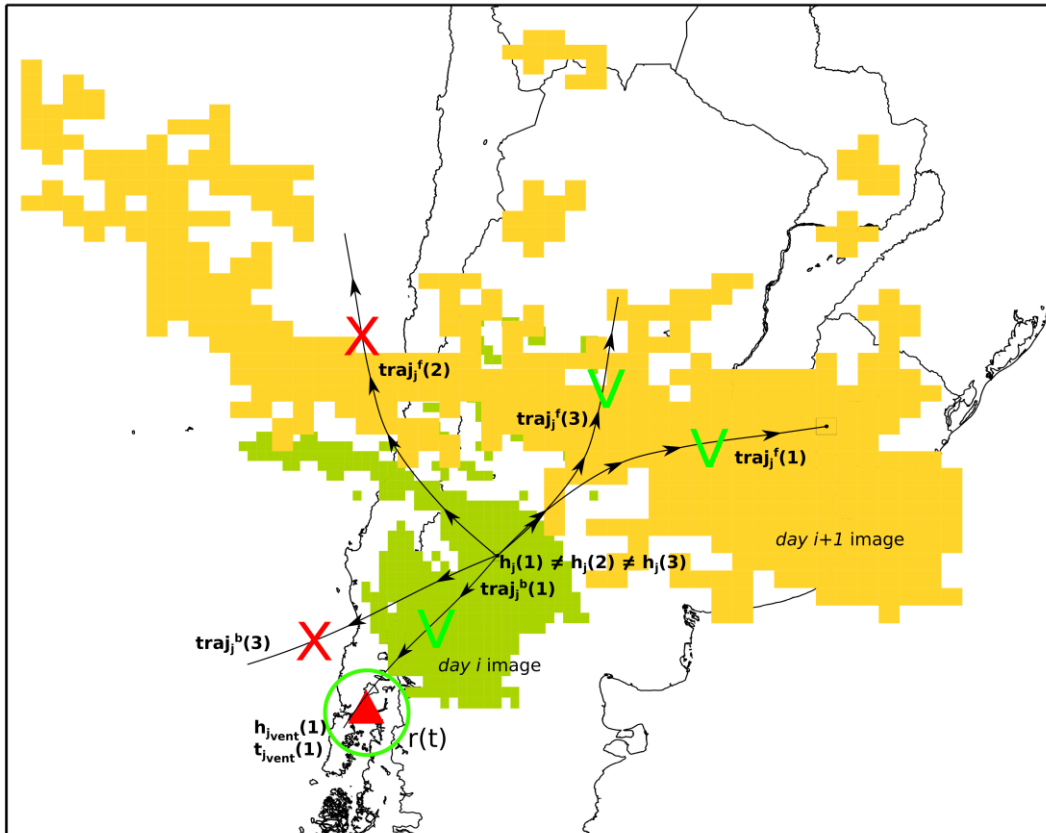
- 20 The research leading to these results has received funding from the European Research Council under the European Union's Seventh Framework Programme (FP/2007–2013)/ERC Grant Agreement no. 279802.

### Author contributions

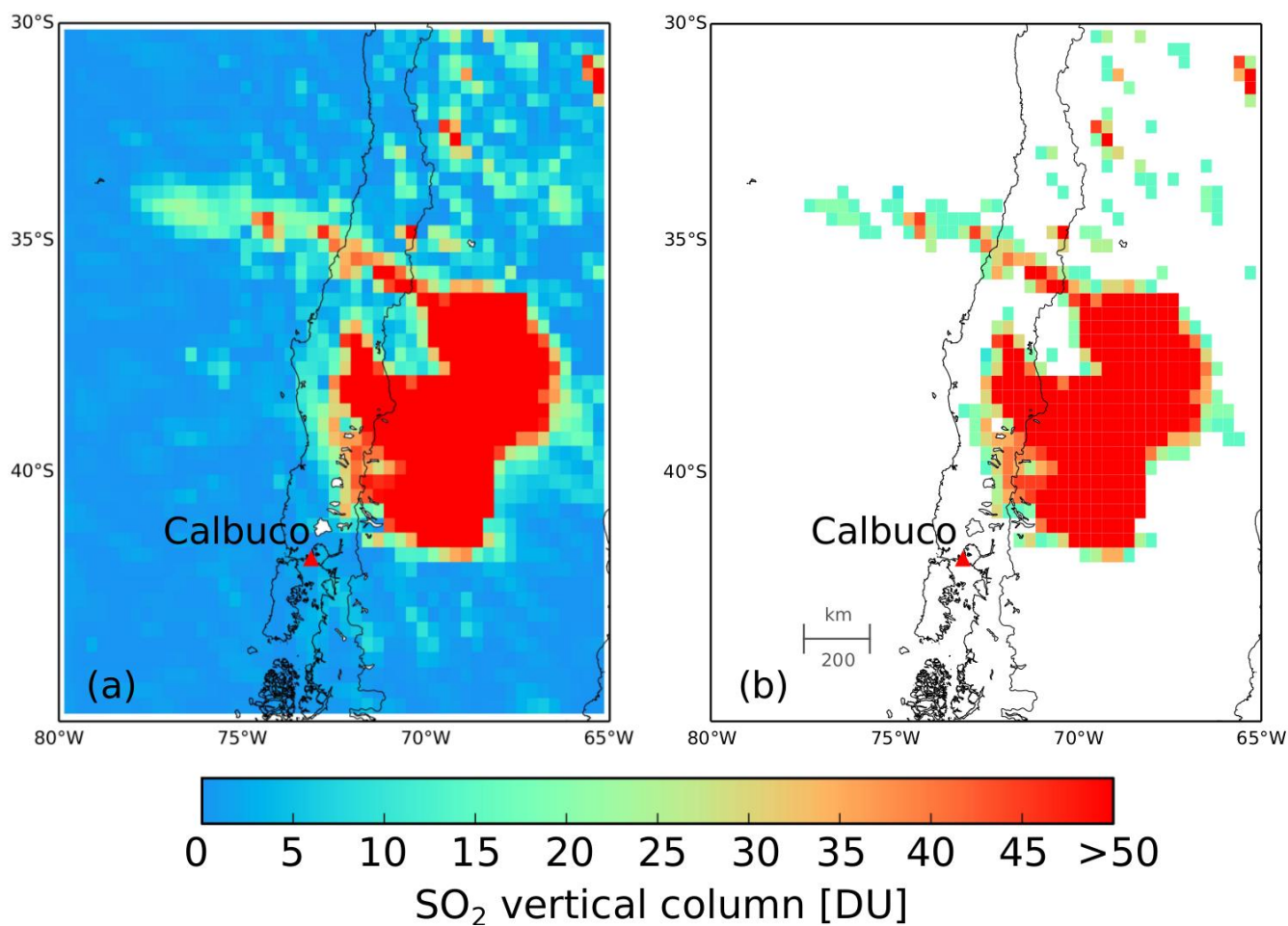
- 25 F.P. and M.B. conceived this work, F.P. produced the numerical code with advice from G.L.S., performed all simulations and produced the manuscript with advice from all co-authors. F.A. contributed to the petrological elements of the paper.



5



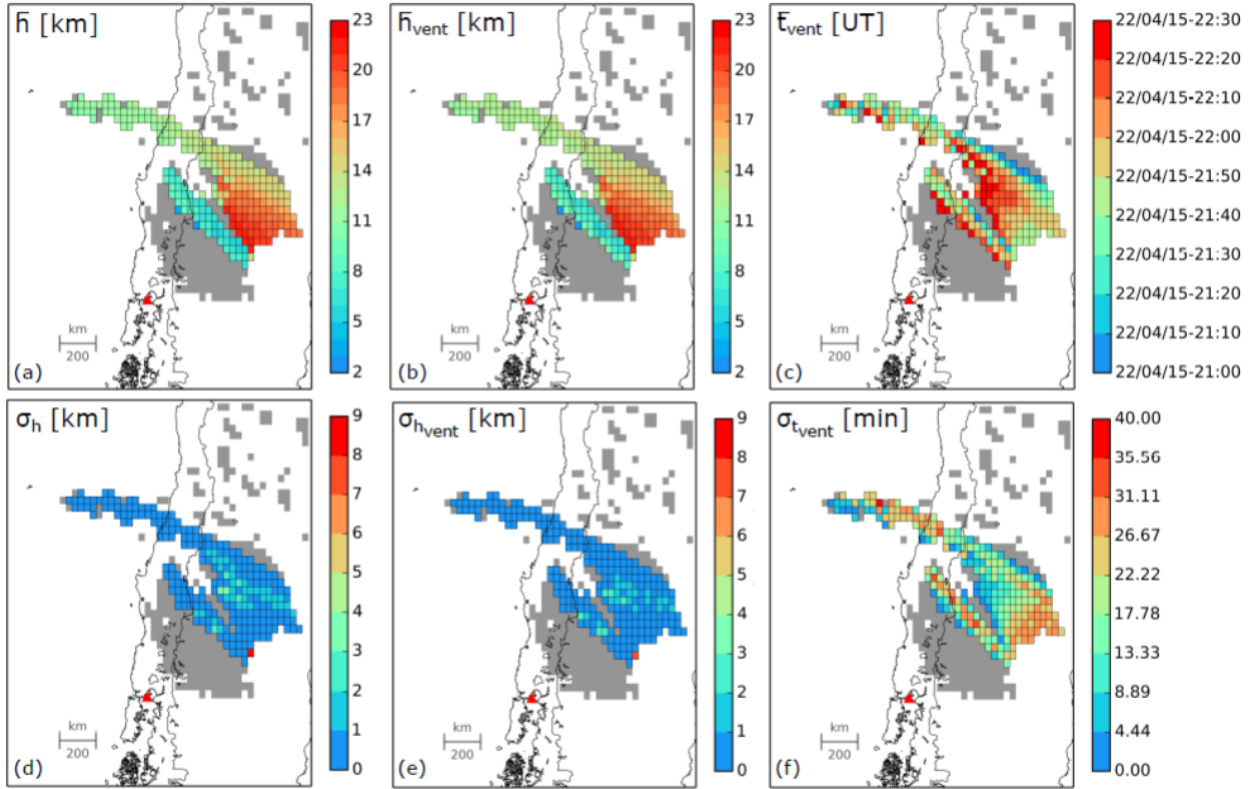
10 **Figure 1.** Schematic representation of the numerical procedure. Green pixels are those associated with the *day i* satellite  
 image, while yellow pixels are those from the *day i+1* image. From pixel *j*, trajectories  $\text{traj}_j^f(1)$ ,  $\text{traj}_j^f(2)$  and  $\text{traj}_j^f(3)$  are run  
 forward from different starting altitudes ( $h_j(1)$ ,  $h_j(2)$  and  $h_j(3)$ ). While  $\text{traj}_j^f(1)$  and  $\text{traj}_j^f(3)$  are consistent with the position of  
 the plume at *day i+1*,  $\text{traj}_j^f(2)$  is not, thus it is neglected. Starting again from pixel *j*,  $\text{traj}_j^b(1)$  and  $\text{traj}_j^b(3)$  are initialized from  
 altitudes  $h_j(1)$  and  $h_j(3)$  and are run backward in time. Only  $\text{traj}_j^b(1)$  is acceptable since it approaches the volcanic vent  
 15 position at a distance less than  $r(t)$ .



5 **Figure 2.** Calbuco SO<sub>2</sub> plume as seen by GOME-2 on 23 April 2015, panel (a). The 2.5 km is used as input for the numerical procedure. Panel (b) presents the volcanic cloud extracted from the background noise.

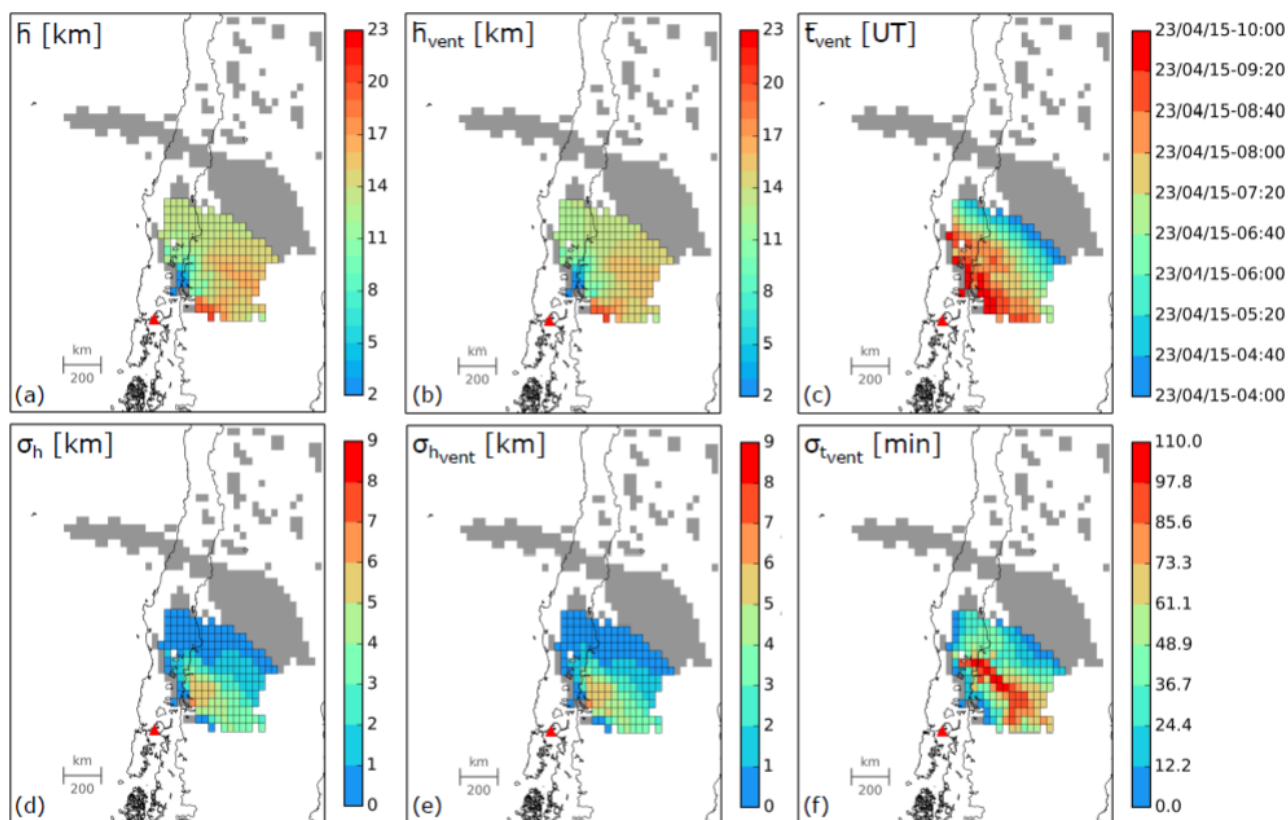
10

15



5

**Figure 3.** Calbuco SO<sub>2</sub> cloud emitted during Eruption 1 (considering trajectories approaching the vent from 21:00 to 22:30 on 22 April 2015). In panels (a), (b), and (c) mean plume height ( $\bar{h}$ ), injection height ( $\bar{h}_{vent}$ ) and injection time ( $\bar{t}_{vent}$ ) are shown. For each pixel  $j$ , these values are computed as:  $\bar{h} = \sum_{i=1}^N \frac{h_j(i)}{N}$ ,  $\bar{h}_{vent} = \sum_{i=1}^N \frac{h_{jvent}(i)}{N}$  and  $\bar{t}_{vent} = \sum_{i=1}^N \frac{t_{jvent}(i)}{N}$ , where  $N$  is the number of trajectories that approach the vent,  $h_j(i)$  is the altitude from which trajectories are initialized, while  $t_{jvent}(i)$  and  $h_{jvent}(i)$  are the time instant and the altitude of approach at vent position. In panels (d), (e) and (f) standard deviations are computed as:  $\sigma_{jh} = \sum_{i=1}^N \frac{(h_j(i) - \bar{h})^2}{N}$ ,  $\sigma_{jh_{vent}} = \sum_{i=1}^N \frac{(h_{jvent}(i) - \bar{h}_{jvent})^2}{N}$  and  $\sigma_{jt_{vent}} = \sum_{i=1}^N \frac{(t_{jvent}(i) - \bar{t}_{jvent})^2}{N}$ . A multi-layered plume emerges, with heights varying from 8 km to more than 20 km. Uncertainties on plume heights appear to be low, mainly between 0 and 1 km.

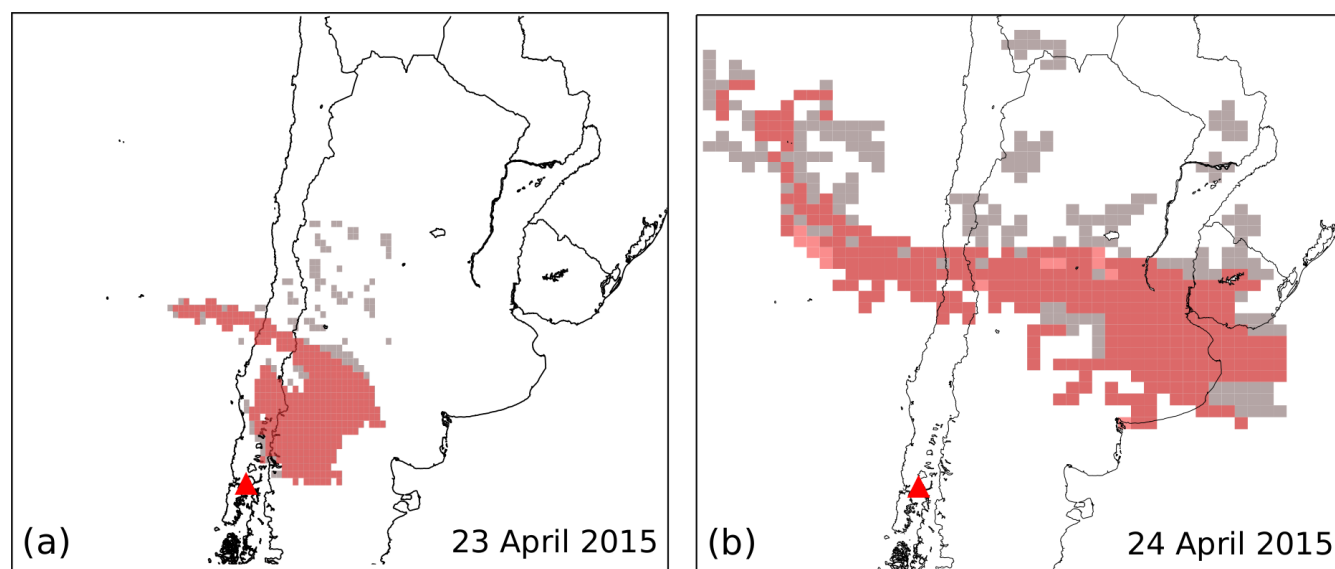


5

**Figure 4.** Calbuco SO<sub>2</sub> cloud emitted during Eruption 2 (considering trajectories approaching the vent from 04:00 to 10:00 on 23 April). Plume heights and injection time are computed as shown for Eruption 1, see Figure 3. The SO<sub>2</sub> cloud appears to be located at ~14 km both at vent location and satellite overpass, panels (a) and (b) with a standard deviation of 2 km, panels (d) and (e). The SO<sub>2</sub> injection time varies from 04:00 for pixels located far from the vent position to 10:00 for those closer, panel (c). Uncertainties on injection time are in the range 0-110 min with a mean value of 45 min, panel (f).

15

20



5

**Figure 5.** Red pixels in panel (a) are those for which at least one backward trajectory is acceptable and thus for which plume height, injection height and injection time can be computed. Grey pixels represent the computational domain. A good coverage for the solution is achieved excluding the sparse pixels located in the northern region of the domain. In panel (b) SO<sub>2</sub> cloud extracted from the 24 April image is shown (grey pixels). Red pixels are those consistent with the endpoints of the forward trajectory simulation performed in order to test the results.

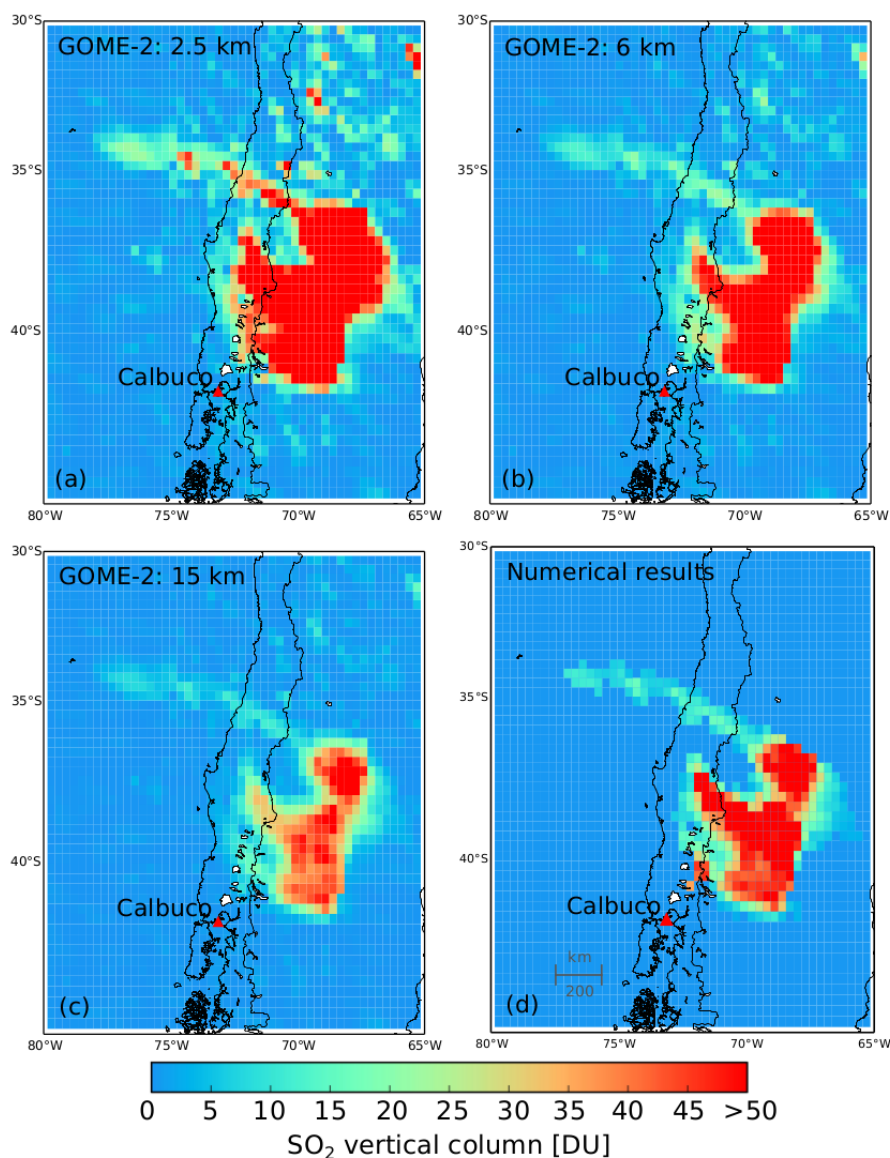
10

15

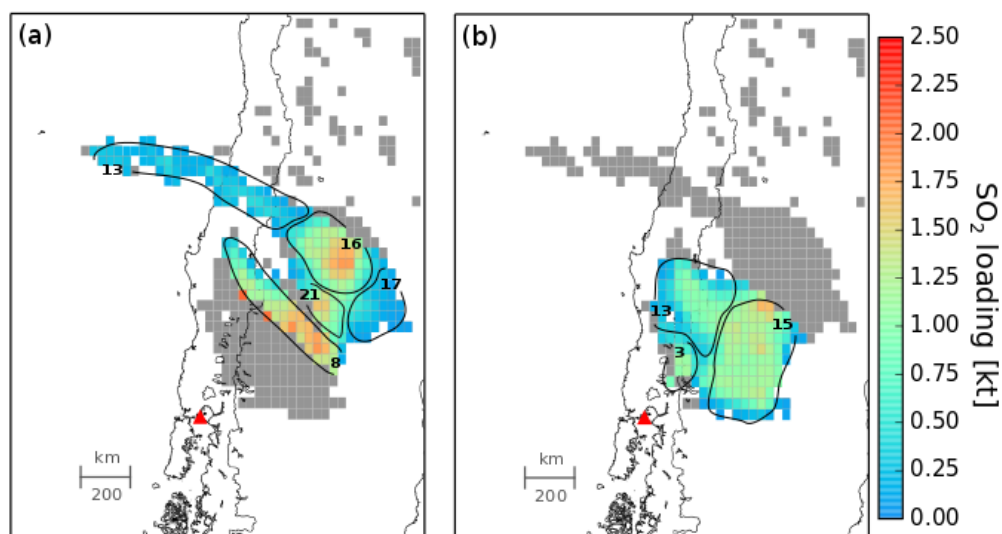
20

25

30



5 **Figure 6.** Vertical columns of Calbuco SO<sub>2</sub> plume as seen on 23 April 2015. Panels (a), (b) and (c) show retrievals performed by GOME-2 assuming plume heights of 2.5 km, 6 km and 15 km respectively. Panel (d) shows column amount corrected with our numerical outcomes on plume height. A good match with the image in panel (c), 15 km retrieval, emerges.



5

**Figure 7.** SO<sub>2</sub> loading computed for each pixel through linear interpolation at the retrieved mean SO<sub>2</sub> height ( $\bar{h}$ ). In panel (a) results for the cloud emitted during Eruption 1 are shown with the bulk of the SO<sub>2</sub> (83% of the total) injected into the atmosphere in the range 8-16 km, while the remain 17% between 17-21 km. Panel (b) presents results for the cloud emitted during Eruption 2. In this case 55% of the SO<sub>2</sub> is injected at 15 km, 41% at 13 km and the 4% at 3 km.

10

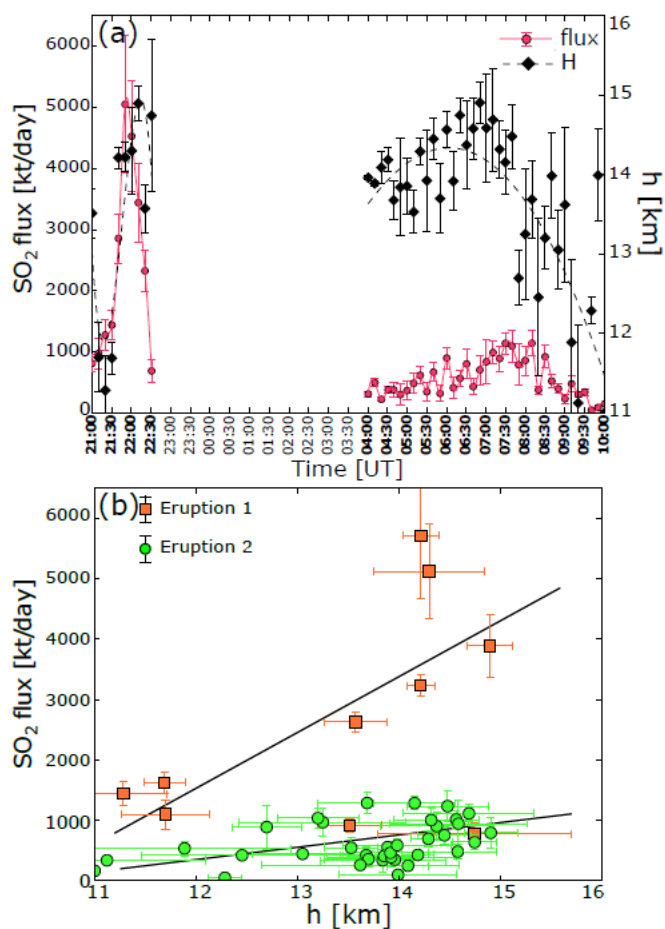


**Figure 8.** Panel (a) shows SO<sub>2</sub> flux time-series together with mean injection height time-series. SO<sub>2</sub> flux as a function of mean injection heights is shown in panel (b).

5

10

15

**Table 1**

	$m(SO_2)_{SAT}$	$DRE$	$S_{MI}$	$S_{gm}$	$m(SO_2)_{PETR}^*$	$m(SO_2)_{ex}^{**}$	% <i>exsolved</i>
<b>E 1</b>	160±30 kt	0.036 km <sup>3</sup>	0.035±0.01wt%	0.009±0.001wt%	38±12 kt	122±28 kt	76±20 %
<b>E 2</b>	140±35 kt	0.10 km <sup>3</sup>	0.04±0.007wt%	0.01±0.003wt%	120±26 kt	20±38 kt	15±28 %

5

\* $m(SO_2)_{PETR} = \rho \cdot DRE \cdot (S_{MI} - S_{gm}) \cdot \frac{MW(SO_2)}{MW(S)} \cdot 0.8$ , where  $\rho = 2450 \text{ kg m}^{-3}$ ,  $MW(SO_2)$  and  $MW(S)$  are the molecular weights of  $SO_2$  and S equal to 64 g mol<sup>-1</sup> and 32 g mol<sup>-1</sup> and 0.8 is a coefficient accounting for 20 vol.% of phenocryst [Castruccio et al., 2016].

\*\* $m(SO_2)_{ex} = m(SO_2)_{SAT} - m(SO_2)_{PETR}$

10

**Table 1:** Calculation of  $SO_2$  budget from Calbuco eruptions.